



Cu Dimer Anchored on C₂N Monolayer: Low-cost and Efficient Bi-atom Catalyst for CO Oxidation

| | |
|-------------------------------|---|
| Journal: | <i>Nanoscale</i> |
| Manuscript ID | NR-ART-04-2018-003394.R2 |
| Article Type: | Paper |
| Date Submitted by the Author: | 26-Jul-2018 |
| Complete List of Authors: | Li, Fengyu; Inner Mongolia University School of Physical Science and Technology, Chen, Zhongfang; University of Puerto Rico, Department of Chemistry |
| | |

**Cu Dimer Anchored on C₂N Monolayer: Low-cost and Efficient
Bi-atom Catalyst for CO Oxidation**

Fengyu Li,^a Zhongfang Chen^{b,*}

^a *School of Physical Science and Technology, Inner Mongolia University, Hohhot,
010021, China*

^b *Department of Chemistry, University of Puerto Rico, Rio Piedras Campus, San Juan,
PR 00931, USA*

*Corresponding Author: zhongfangchen@gmail.com

Abstract

By means of density functional theory (DFT) computations, we systemically investigated the CO/O₂ adsorption and CO oxidation pathways on the bi-atom catalyst, namely the copper dimer anchored on C₂N monolayer (Cu₂@C₂N), in comparison with its monometallic counterpart Cu₁@C₂N. Cu dimer can be stably embedded in the porous C₂N monolayer. The reactions between the adsorbed O₂ with CO via both bi-molecular and tri-molecular Langmuir–Hinshelwood (LH) and Eley–Rideal (ER) mechanisms were comparably studied, and we found that bi-atom catalyst Cu₂@C₂N possesses superior performance toward CO oxidation compared to single-atom catalyst Cu₁@C₂N. Our comparative study suggests that the newly predicted bi-atom catalyst (copper dimer anchored on suitable support) is highly active for CO oxidation, which could provide a useful guideline for further developing highly effective and low-cost green nanocatalysts.

1. Introduction

The CO oxidation, an example of a benchmark catalytic reaction in heterogeneous catalysis, plays a very important role in the environmental protection and the removal of CO contaminations from H₂-rich fuel gases for polymer electrolyte fuel cells (PEFC)¹ among many other industrial processes.

Typically supported metal clusters, especially those made of noble metals, e.g., Pt, Pd, Au, Rh and Ru, are widely used as catalysts for the CO oxidation. However, the catalytic activities of the supported metal nanoparticles can be strongly size- and shape-dependent,²⁻⁴ moreover, the overall efficiency has been rather low on a per metal atom basis since only the surface atoms are active for catalysis. To reduce the metal usage in catalysis and enhance the catalytic efficiency, the single-atom catalysts (SACs)⁵⁻¹³ have become a hot topic in recent years. The single-atom catalyst contains only isolated individual atoms dispersed on, and/or coordinated with, the surface atoms of an appropriate support, which maximizes the metal atom efficiency. So far, various SACs have been successfully fabricated, and are highly active for a variety of catalytic reactions. For example, in 2011 Zhang and coworkers successfully deposited single Pt atoms on iron oxide surface, experimentally demonstrated its high activity towards CO oxidation, and theoretically elucidated its reaction mechanism.⁵ Afterwards, they fabricated single Au/Pt/Ir/Ni atoms on the other oxide surfaces such as FeO_x,¹⁴⁻²⁰ Co₃O₄,²¹ and CeO₂,²²; other experimental groups loaded single Pt and Os atoms on Al₂O₃,²³ and MgO²⁴ surfaces. The successful fabrication of single Au/Pt/Ir/Ni atoms on the FeO_x surface also inspired many theoretical efforts to develop SACs. Among others, we systemically examined the stability and catalytic performance of various FeO_x-supported single atom catalysts for CO oxidation by means of density functional theory (DFT) computations,²⁵ Liang *et al.* provided a

comprehensive fundamental understanding to the stability and activity trends the FeO_x-based SACs with the 3d, 4d, and 5d metals of group VIII to IB for CO oxidation.²⁶ SACs could be highly active towards many important reactions such as CO oxidation, hydrogenation of nitroarenes, NO reduction, and water-gas-shift reaction.

In recent years, scientists have extended the enthusiasm on graphene to other two-dimensional (2D) materials:²⁷⁻³⁵ A variety of porous graphene-like materials such as g-C₃N₄,³⁶ graphyne,³⁷ graphdiyne,³⁸ and C₂N³⁹ were synthesized; through “bottom-up” technique, many 2D organometallic sheets, such as Fe-phthalocyanine (Fe-Pc),⁴⁰ Fe-1,3,5-tris(pyridyl)benzene,⁴¹ and Ni- bis(dithiolene)⁴² were fabricated. These 2D materials exhibit great potential in applications for gas separation, energy storage, bio-sensors, etc. In particular, the porous 2D materials can be used as the substrates to anchor metal atoms/clusters in catalysis. Among others, single metal atoms (Pt, Pd, Ag, Ir, Au) embedded in g-C₃N₄ are highly active for the semihydrogenation of 1-hexyne;⁴³ Co₁@C₂N and Ni₁@C₂N computationally designed by Jiang’s group could serve as low-cost but highly efficient catalysts for oxygen evolution reaction;⁴⁴ Ma *et al.* theoretically predicted that noble atoms anchored on graphyne and 3d transition metal atoms embedded on C₂N monolayer are very promising for low-temperature CO oxidation.^{45, 46} Zhao and coworkers computationally screened a series of single transition metal atoms on C₂N monolayer as electrocatalysts for nitrogen reduction reaction (NRR), and found that Mo@C₂N possesses the best NRR catalytic performance.⁴⁷ Wang *et al.* predicted that the experimentally available 2D Fe-Pc monolayer with precisely-controlled distribution of Fe atoms is a promising catalyst for oxygen reduction reaction (ORR),⁴⁸ shortly Wang *et al.* synthesized Fe-Pc monolayer on conductive nanotubes and demonstrated

its excellent ORR activity.⁴⁹

Note that metal-metal bonds play a very important role in catalysis.⁵⁰ However, metal-metal bonding often competes with the metal-ligand bonding, consequently, under catalytic conditions, mononuclear and dinuclear species may coexist and rapidly interconvert to each other. Thus, typically the dinuclear metal units are fixed for further catalytic performance evaluations. For example, Matsushita *et al.* successfully synthesized expanded Pc congeners with two Mo or W central metal ions under normal Pc formation reaction conditions,⁵¹ this achievement inspired Shen *et al.*'s computational investigation on CO₂ electroreduction performance of expanded phthalocyanine sheets with different transition metal dimers, which singled out Mn dimer as the best active center.⁵² He *et al.* realized the synthesis of Fe dimers embedded within graphene vacancy defects,⁵³ but the catalytic performance of graphene supported metal dimers has not been examined. Very recently, Lu, Wei and coworkers realized bottom-up precise synthesis of stable platinum dimers (but dominantly in the oxidized form of Pt₂O_x without Pt–Pt bond) on graphene using atomic layer deposition, and showed that Pt₂ dimers exhibit a striking activity towards hydrolytic dehydrogenation of ammonia borane, which is ~17- and 45-fold higher than that of graphene supported Pt₁ single atoms and nanoparticles.⁵⁴ Li *et al.* theoretically designed ORR catalyst based on double transition metal (TM) atoms stably supported by 2D crystal C₂N, and showed that the catalytic performance is better than their single-atom counterparts.⁵⁵

Inspired by these remarkable progress in the syntheses of metal dimers anchored in 2D materials and their great potential as low-cost, high-performance catalysts, in this work, by means of systematic density functional theory (DFT) computations, we examined the stability and electronic properties of copper dimers anchored on the

porous C₂N monolayer³⁹ (Cu₂@C₂N), and explored its catalytic behavior for CO oxidation in comparison with the monometallic counterpart (Cu₁@C₂N). Our computational results showed that the bi-atom Cu₂@C₂N catalyst has a high stability and superior performance toward CO oxidation compared to the single-atom Cu₁@C₂N catalyst. This work not only spans the single-atom catalysts to bi-atom catalysis, but also provides insights and guidelines to experimentalists, and help promote the design and production of novel low-cost and efficient nanocatalysts.

2. Computational Details

Our spin-polarized DFT computations were based on the generalized gradient approximation (GGA) in the form of the Perdew-Burke-Ernzerhof exchange-correlation functional (PBE).⁵⁶ Frozen-core all-electron projector augmented wave (PAW) method⁵⁷ was used as implemented in the Vienna *ab initio* simulation package (VASP).⁵⁸ The Monkhorst-Pack scheme⁵⁹ of (5×5×1) k-points mesh was applied to carry out the numerical integrations in the reciprocal space. The kinetic energy cutoff for the plane-wave basis set was chosen to be 500 eV. The optimized lattice parameter of the 2D C₂N unitcell (C₁₂N₆) is 8.33 Å, which agrees well with both experimental value³⁹ and previous theoretical results.⁴⁶ The computations on the isolated molecules and atoms were carried out in a (10 Å × 10 Å × 10 Å) unit cell with the Γ -point only for the *k*-point sampling. The reaction pathways were investigated by using the nudged elastic band method (NEB),⁶⁰ and for each reaction, nine images were inserted between the reactant and the product. Bader charge analysis⁶¹ was used to evaluate the charge transfer.

The binding energy (E_b) of a metal atom or the adsorption energy (E_{ad}) of an adsorbate (O₂, CO, etc.) on the substrate was defined as $E_b/E_{ad} = E + E' - E_{tot}$, where

E , E' and E_{tot} represent the total energies of the clean slab, the isolated adsorbed atom/molecule, and the slab after adsorption, respectively. In the case of the co-adsorption of two species A and B, E' is the sum of the total energies of isolated A and B. According to this definition, a positive (negative) value of E_b/E_{ad} indicates that the adsorption is exothermic (endothermic).

3. Results and Discussion

3.1. Geometries and Stabilities of the $\text{Cu}_1@C_2N$ and $\text{Cu}_2@C_2N$ monolayers.

We first considered all the possible anchored sites for single Cu atom on C_2N monolayer, i.e., the pore site P1 (at which Cu_1 coordinates with three N atoms), P2 (at which Cu_1 coordinates with two N atoms) and P3, the hollow site H1 and H2, and the bridge site B1, B2 and B3 (B3 site is not stable, it will change to P2 site upon geometry optimization), as illustrated in Figure 1. The binding energies of Cu atom at the three pore sites are much more favorable than the hollow and bridge sites (see Table 1), and among the pore sites, P2 has the largest binding energy (3.25 eV), which is similar to previous theoretical results.^{46,49} Though the largest Cu binding energy is slightly smaller than the cohesive energy of Cu bulk (3.47 eV) computed at the same level of theory, the sharp difference (> 3 eV) of the binding energies between the stable pore site and adjacent hollow/bridge site implies that the diffusion barrier of Cu_1 on C_2N is higher than 3 eV and the Cu atom aggregation can be avoided.

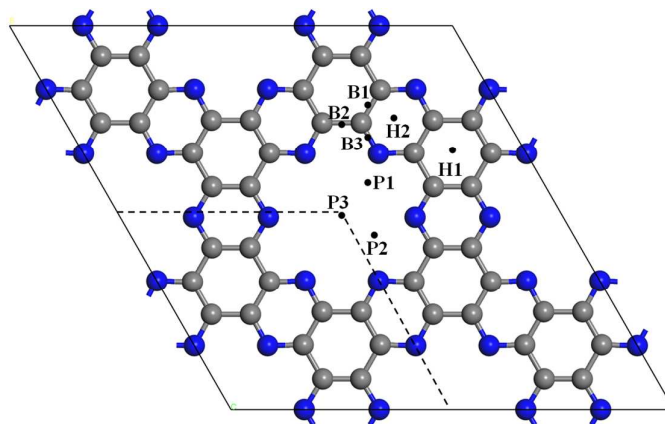


Figure 1. Top view of the 2×2 C₂N monolayer and the considered adsorption sites for Cu₁ atom. Color scheme: C, gray; N, blue.

Energetically the Cu₂ dimer prefers to anchor on two equivalent pore sites P1P1 ($E_b = 6.02$ eV) and P2P2 ($E_b = 5.94$ eV) (Figure 2), and the nonequivalent pore sites will transfer to the equivalent ones (the P1P2 and P2P3 will change to P1P1 and P2P2, respectively). To evaluate the binding strength of the second Cu atom, we used dimer energy⁶² which can be defined as the binding energy of Cu₂ dimer subtracting the binding energy of Cu₁ atom anchored on C₂N. As shown in Table 1, the dimer energy of the second Cu atom to form the P1P1 ($E_{\text{dim}} = 2.82$ eV) or P2P2 ($E_{\text{dim}} = 2.69$ eV) configuration is (> 2 eV) stronger than the dimer energy (~ 0.54 eV) of the Cu₂ dimer with one Cu at the pore site and one Cu atom at the hollow/bridge site, which indicates the prohibition of Cu diffusion and further clustering.

Our above discussions showed that both Cu₁@C₂N and Cu₂@C₂N monolayers have good thermodynamic stabilities. The Cu₁ ($a = 8.26$ Å, $b = 8.31$ Å for P2 site) and Cu₂ ($a = 8.64$ Å, $b = 8.17$ Å for P1P1 site) adsorption breaks the symmetry and induces the lattice deformation of C₂N ($a = b = 8.33$ Å). Compared to the purely planar Cu₁@C₂N (Figure 2a), the additional Cu atom in Cu₂@C₂N monolayer slightly distorts the plane, and the two Cu atoms are above and below the plane respectively

(Figure 2b,c). According to Bader charge analysis, in the $\text{Cu}_1@C_2N$ monolayer, Cu_1 at the pore sites ($+0.72 \sim +0.77 |e|$) is more positively charged than that at hollow or edge sites ($+0.30 \sim +0.39 |e|$); In comparison, the total electron transfer between Cu_2 dimer at pore sites and the C_2N monolayer substrate are much enhanced ($1.22, 1.24 |e|$ for P1P1 and P2P2, respectively), but the charge transfer per Cu atom in $\text{Cu}_2@C_2N$ monolayer is $\sim 0.15 |e|$ less than that in $\text{Cu}_1@C_2N$ monolayer (Table 1).

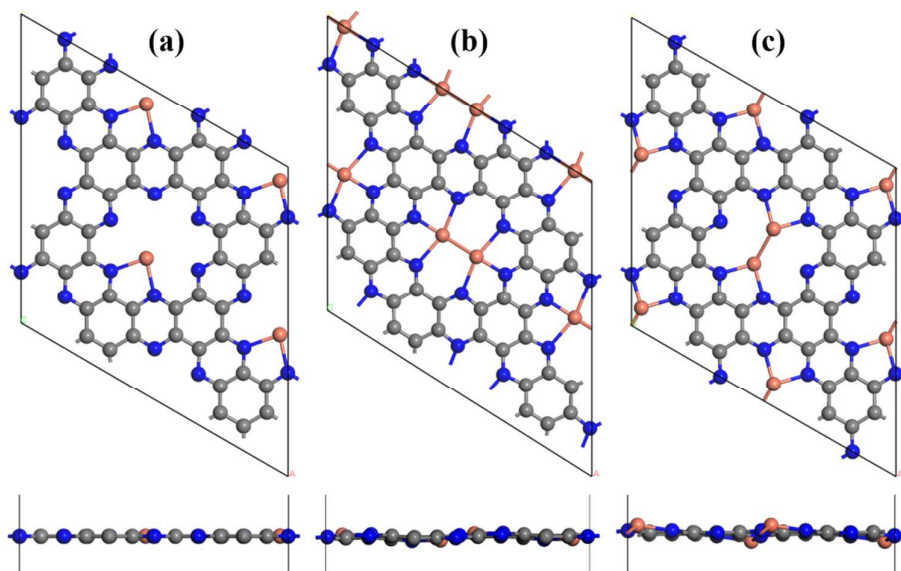


Figure 2. Top and side views of the 2×2 $\text{Cu}_1@C_2N$ with Cu at P2 site (a), $\text{Cu}_2@C_2N$ with Cu_2 at P1P1 site (b), and $\text{Cu}_2@C_2N$ with Cu_2 at P2P2 site (c). Color scheme: Cu, orange; C, gray; N, blue.

Table 1 The binding energies (E_b , eV) and charge transfer (q , e) of Cu_1 and Cu_2 at different sites, as well as the dimer energies (E_{dim} , eV) Cu_2 .

| | | Cu_1 | | | | | | | | |
|------------------|--|---------------|------|---------------|---------------|------|------|------|---------------|---------------|
| | | P1 | P2 | P3 | H1 | H2 | B1 | B2 | B3→P2 | |
| E_b | | 3.20 | 3.25 | 2.86 | 0.03 | 0.30 | 0.39 | 0.33 | 3.25 | |
| q | | 0.76 | 0.77 | 0.72 | 0.39 | 0.31 | 0.33 | 0.30 | 0.77 | |
| | | Cu_2 | | | | | | | | |
| | | P1P1 | P2P2 | P1P2 →P1P1 | P2P3 →P2P2 | P2H1 | P2H2 | P2B1 | P2B2 →P2H1 | P2B3 →P2H2 |
| E_b | | 6.02 | 5.94 | 6.02 | 5.94 | 3.80 | 3.79 | 3.80 | 3.80 | 3.79 |
| E_{dim} | | 2.82 | 2.69 | 2.82 | 2.69 | 0.55 | 0.54 | 0.55 | 0.55 | 0.54 |
| | | 0.62 | 0.61 | 0.62 | 0.61 | 0.77 | 0.77 | 0.77 | 0.77 | 0.77 |
| q | | 0.63 | 0.61 | 0.63 | 0.61 | 0.23 | 0.22 | 0.21 | 0.23 | 0.22 |

3.2. Adsorption of CO and O₂ molecules on the $\text{Cu}_1@C_2N$ and $\text{Cu}_2@C_2N$ monolayers.

Starting from the most stable structures of $\text{Cu}@C_2N$ and $\text{Cu}_2@C_2N$ shown in Figure 2a and Figure 2b, we examined many adsorption sites in order to find out the energetically most favorable adsorption configuration for each adsorbate (CO, O₂, or CO/O₂ coadsorption). Since the Cu_2 dimer anchored at P1P1 site simultaneously moves to P2P2 site when it is adsorbed by O₂ or CO (Figure S1), thus the model of $\text{Cu}_2@C_2N$ with Cu_2 at P2P2 site (Figure 2c) was used to investigate the CO oxidation process. Table 2 presents the adsorption energies and the key structural parameters of the CO and O₂ complexes on $\text{Cu}_2@C_2N$ monolayer.

Table 2 The CO and O₂ binding energies (E_{ad} , eV) on Cu₁@C₂N and Cu₂@C₂N, their corresponding bond lengths ($d_{\text{C-O}}/d_{\text{O-O}}$, Å), as well as the Bader charge (q , |e|) of CO/O₂ and Cu₁/Cu₂.

| | CO | | | | O ₂ | | | |
|-----------------------------------|-----------------|------------------|-----------------|-----------------|-----------------|------------------|-----------------|------------------|
| | E_{ad} | $d_{\text{C-O}}$ | q_{Cu} | q_{CO} | E_{ad} | $d_{\text{O-O}}$ | q_{Cu} | q_{O_2} |
| Cu ₁ @C ₂ N | 1.46 | 1.15 | +0.83 | -0.13 | 0.59 | 1.28 | +0.95 | -0.38 |
| Cu ₂ @C ₂ N | 2.14 | 1.18 | +0.78 +0.75 | -0.34 | 1.33 | 1.45 | +0.99 +0.99 | -0.90 |

For CO adsorption on both Cu₁@C₂N and Cu₂@C₂N monolayers, the most favorable structure (Figure 3a,b) adopts an end-on configuration (in which the O–C bond points to the Cu atom with a tilt angle perpendicular to the C₂N substrate). The C–O bond lengths (1.15 and 1.18 Å on Cu₁@C₂N and Cu₂@C₂N, respectively) of the adsorbed CO are slightly elongated compared to that of the isolated CO molecule (1.14 Å). The adsorption energies of CO on Cu₁@C₂N and Cu₂@C₂N are 1.46 and 2.14 eV, respectively.

Beware of the deficiency in describing van der Waals interactions of the generalized gradient approximation (GGA), the BEEF-vdW⁶³ corrected PBE was further employed for CO and O₂ adsorption on Cu₁@C₂N and Cu₂@C₂N, as well as the O₂ dissociation on Cu₂@C₂N. Our computations revealed that the BEEF-vdW functional gave very similar results as PBE: the binding energy of CO is larger than that of O₂ on both Cu₁@C₂N and Cu₂@C₂N by 0.59 (0.87) and 0.54 (0.81) eV at with (without) BEEF-vdW correction, respectively; the O₂ dissociation on Cu₂@C₂N requires to overcome a barrier of 0.52 eV at the BEEF-vdW-PBE level, which is quite close to the results of PBE (0.50 eV) and PBE-D2⁶⁴ (0.56 eV⁴⁴). Therefore, the PBE

method was adopted for all computations in our study.

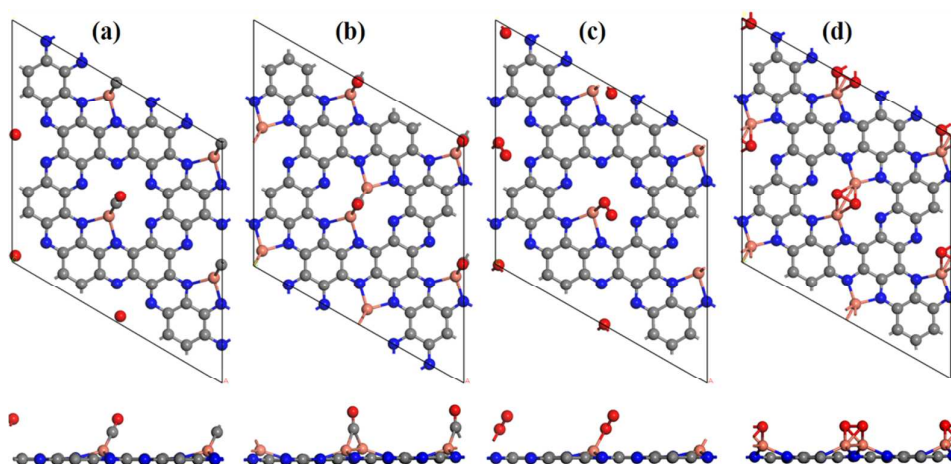


Figure 3. Top and side views of CO adsorption on $\text{Cu}_1@C_2N$ (a) and $\text{Cu}_2@C_2N$ (b), and O_2 adsorption on $\text{Cu}_1@C_2N$ (c) and $\text{Cu}_2@C_2N$ (d). Color scheme: Cu, orange; C, gray; N, blue; O, red.

On $\text{Cu}_1@C_2N$ monolayer, O_2 adsorption adopts an end-on configuration in the energetically most favorable pattern with the adsorption energy of 0.59 eV (Figure 3c), while on $\text{Cu}_2@C_2N$ monolayer, the most favorable configuration is characterized by O_2 “parallel” to C_2N sheet (side-on configuration) with an adsorption energy of 1.33 eV (Figure 3d). In contrast to the slightly lengthened O–O bond length (d_{O-O}) of the adsorbed O_2 on $\text{Cu}_1@C_2N$ (1.28 Å), the d_{O-O} of the adsorbed O_2 molecule is elongated by about 0.22 Å on $\text{Cu}_2@C_2N$ (1.45 Å).

To gain deeper insight into the interaction between CO/ O_2 molecule and the substrates, we analyzed the atomic charges and the electronic structures of these systems. In general, the charge transfer between the adsorbate and substrate is more pronounced on $\text{Cu}_2@C_2N$ than that on $\text{Cu}_1@C_2N$: the adsorbed CO extracts 0.34 and 0.13 e^- from $\text{Cu}_2@C_2N$ and $\text{Cu}_1@C_2N$, respectively; the adsorbed O_2 extracts 0.38 e^-

from $\text{Cu}_1@C_2N$, while $0.90 e^-$ from $\text{Cu}_2@C_2N$. By analyzing partial density of states (PDOS) (Figure 4), we found that there is more hybridization between $3d$ states of Cu and $2p$ states of CO/O₂ for $\text{Cu}_2@C_2N$ monolayer. The more significant charge transfer and stronger couplings between the adsorbates and the $\text{Cu}_2@C_2N$ monolayer, as compared with those on $\text{Cu}_1@C_2N$ monolayer, are responsible for the higher binding strength of the embedded Cu₂ dimer with CO/O₂.

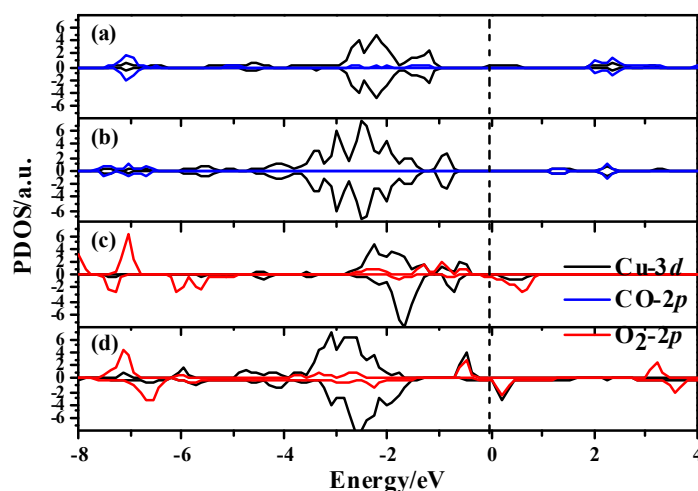


Figure 4. Partial density of states (PDOS) of CO adsorption on $\text{Cu}_1@C_2N$ (a) and $\text{Cu}_2@C_2N$ (b), and O₂ adsorption on $\text{Cu}_1@C_2N$ (c) and $\text{Cu}_2@C_2N$ (d). The Fermi level was set to be zero as denoted by the black dashed line.

We also considered the coadsorption of CO and O₂ molecules on both $\text{Cu}_1@C_2N$ and $\text{Cu}_2@C_2N$ systems. On $\text{Cu}_1@C_2N$, the coadsorption energy (0.53 eV) of CO and O₂ is even less than the adsorption energy of individual O₂ molecule (0.59 eV), indicating strong repulsion between the coadsorbed CO and O₂ molecules, which can also be confirmed by the elongated intermolecular distance of CO and O₂ as well as the lengthened distance between CO and Cu after geometry optimization (Figure S2).

In contrast to the strong repulsion between the coadsorbed CO and O₂ on Cu₂@C₂N, the coadsorption of CO and O₂ on Cu₂@C₂N is energetically favorable: the coadsorption energy (1.50 eV) is larger than the sole O₂ adsorption energy (1.33 eV). The repulsion between the coadsorption of CO and O₂ molecules can be understood in the competing of the limited number of *d* orbitals in Cu₁@C₂N, while the Cu₂@C₂N can provide more *d* orbitals to hybridize with both O₂-*p* and CO-*p* orbitals, resulting in an exothermic process.

We tried to use the *d*-band center theory^{65–68} to explain the remarkable difference in the adsorption strength of CO/O₂ on the Cu₁@C₂N and Cu₂@C₂N, our computations revealed that the *d*-band center of Cu₂@C₂N blue-shifts (moving to lower energy region) compared to that of Cu₁@C₂N (Figure S3), which does not agree with the *d*-band center theory. The confliction with the *d*-band center theory was reported before.^{69,70} Note that the pre-assumption of the *d*-band center theory is that the *s* and *p* states of the metal surfaces are comparable,^{65,67} while for the case of metal clusters, the electron states become delocalized, and contributions beyond *d*-band center should be considered, such as the coordination number, the electronegativity and electronegativity of the nearest neighborings.⁷¹ We further plotted the density of Cu-*s* and Cu-*p* states of Cu₁ and Cu₂, and found that both Cu-*s* and Cu-*p* states Cu₂ exhibit blue shifts as well compared to Cu₁ (Figure S4), moreover, the Cu-*s* and Cu-*p* orbitals also hybridize with the orbitals of the adsorbate (Figure S5), helping enhance the adsorption on Cu₂@C₂N.

3.3. Mechanisms of CO Oxidation on the Cu₁@C₂N and Cu₂@C₂N monolayers.

Noting that the CO adsorption energy is larger than that of O₂, to avoid the CO poisoning issue, we used the O₂-preadsorbed Cu₁@C₂N and Cu₂@C₂N to further

examine the mechanisms of CO oxidation over these two catalysts.

We first consider the CO oxidation on $\text{Cu}_1@C_2N$. According to the repulsion of CO and O_2 coadsorption on $\text{Cu}_1@C_2N$ (Figure S2), we only examined the Eley-Rideal (E-R) mechanism for the first CO_2 production. As the CO molecule approaches the O_2 adsorbed on $\text{Cu}_1@C_2N$ with end-on configuration, the O–O bond length becomes longer (from 1.28 Å in S2, to 1.30 Å in S3, and finally broken to 3.24 Å when the first CO_2 is formed, S4, in Figure 5), the intermolecular distance of C and O becomes shorter (from 2.96 Å in S2, to 2.52 Å in S3, and finally to 1.17 Å when the first CO_2 is generated, S4, in Figure 5). It has to overcome a barrier of 0.53 eV for the first CO_2 formation via E-R mechanism, releasing the heat of 1.88 eV.

The removal of the O on the $\text{Cu}_1@C_2N$ to finalize the reaction cycle was examined via both Langmuir-Hinshelwood (L-H) and E-R mechanism. However, similar to the case of coadsorption of CO and O_2 , the CO is repulsed by the pre-adsorbed O^* : the distance between C of CO and O^* is 3.42 Å, and the adsorption energy of CO is as weak as 0.08 eV. Therefore, the L-H process was not further studied. In the E-R reaction route, the CO approaches to the O^* (S5 in Figure 5), passing over the transition state (S6 in Figure 5) to form the second CO_2 (S7 in Figure 5). The E-R step only requires an energy barrier of 0.21 eV with the exothermicity of 3.51 eV.

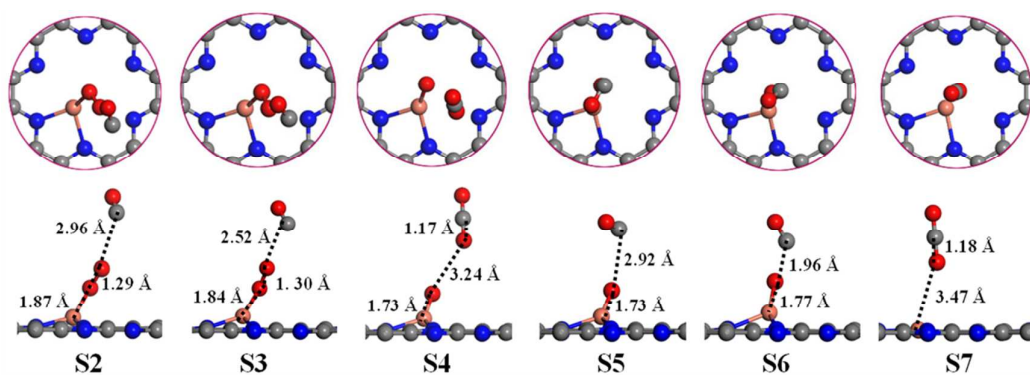


Figure 5. Atomic configurations of S2-S7 and the key structural parameters for CO oxidation via E-R mechanism on $\text{Cu}_1@C_2N$. The corresponding energy profiles were given in Figure 6 as marked in pink. Color scheme: C, gray; N, blue; O, red; Cu, orange.

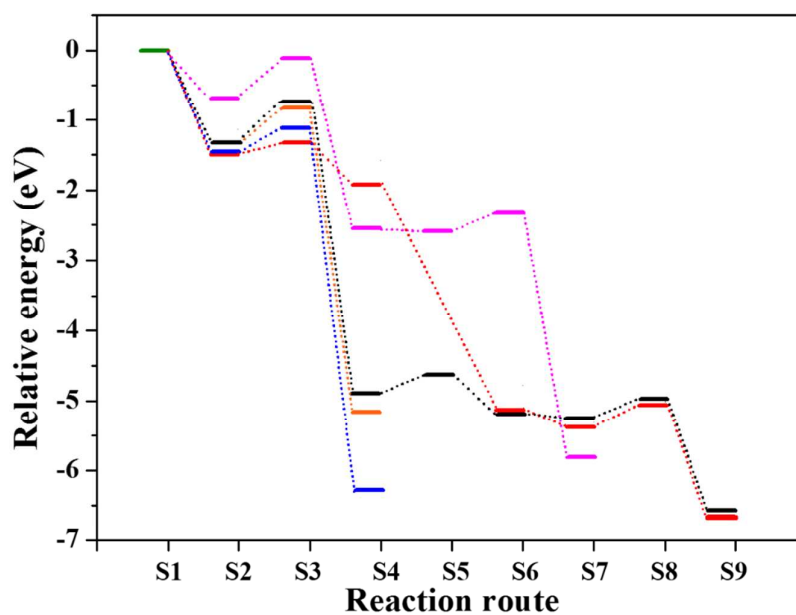


Figure 6. Energy profiles for CO oxidation with O_2 on Cu_1 - and Cu_2 -anchored C_2N monolayers. The pink, black, orange, red and blue lines denote the E-R route on $\text{Cu}_1@C_2N$, E-R-1, E-R-2, L-H, and T-E-R route on $\text{Cu}_2@C_2N$, respectively, corresponding to the structures shown in Figure 5, 7-10.

For CO oxidation on $\text{Cu}_2@\text{C}_2\text{N}$, we first investigated the bi-molecular L-H mechanism, then examined both bi-molecular and tri-molecular E-R mechanisms.

For the L-H mechanism, the reaction starts from the O_2 and CO coadsorption on $\text{Cu}_2@\text{C}_2\text{N}$ (S2 in Figure 7), where the adsorbed O_2 (O-O^*) and OC (OC^*) adopt the side-on and end-on configuration, respectively. As discussed above, the coadsorption is energetically favorable. Then, OC^* approaches to O-O^* passing over the transition state S3 (Figure 7) with a barrier of 0.17 eV to form the intermediate OOCO^* (S4 in Figure 7), and subsequently the first CO_2 is released barrierlessly, leaving the unreacted O atom of O_2 attached to the center of Cu_2 ($\text{S4} \rightarrow \text{S5} \rightarrow \text{S6}$ in Figure 7). The process for the second CO to adsorb on the O^* (S7 in Figure 7) is slightly exothermic (0.11 eV). It has to overcome a barrier of 0.31 eV (S8 in Figure 7) to produce the second CO_2 molecule (S9 in Figure 7). The OOCO^* formation, as well as the first and second CO_2 formation via L-H mechanism, are exothermic by 0.44, 3.20 and 1.28 eV, respectively. The calculated adsorption energies of the first and second physisorbed CO_2 molecule are 0.08 and 0.03 eV, respectively, indicating the facile removal of the produced CO_2 molecules.

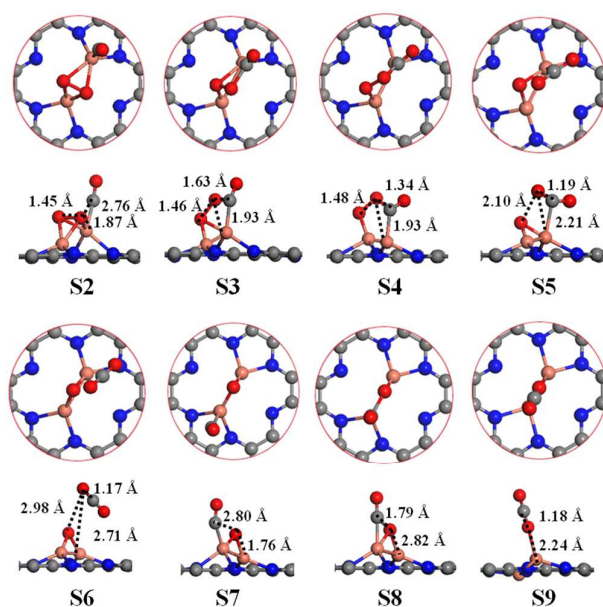


Figure 7. Atomic configurations of S2-S9 and the key structural parameters for CO oxidation via L-H mechanism on Cu₂@C₂N. The corresponding energy profiles are given in Figure 6 as marked in red. Color scheme: C, gray; N, blue; O, red; Cu, orange.

For the bi-molecular E-R mechanism, we examined two pathways for the first CO₂ formation. In the first reaction pathway (E-R-1, the black route in Figure 6 and atomic configurations in Figure 8), CO approaches the adsorbed O₂ to form a metastable carbonate-like intermediate state (S4 in Figure 8) (O-O distance 2.19 Å) by passing a transition state in which O-O is elongated to 2.19 Å. This process is quite similar to the reaction of CO with O₂ over some single-atom catalysts Au/Cu/Fe-embedded graphene⁷²⁻⁷⁴ and Fe-anchored graphene oxide.⁷⁵ The process of the carbonate-like intermediate (S4 in Figure 8) formation is exothermic by 3.55 eV, but due to the breaking of an O-O bond and the formation of new C-O bonds, the activation barrier (0.59 eV) is relatively high, thus this pathway is not kinetically favorable. Following the formation of the carbonate-like intermediate (S4 in Figure 8),

crossing a barrier of 0.26 eV (S5 in Figure 8) and releasing 0.33 eV of heat, the first CO_2 is produced (S6 in Figure 8).

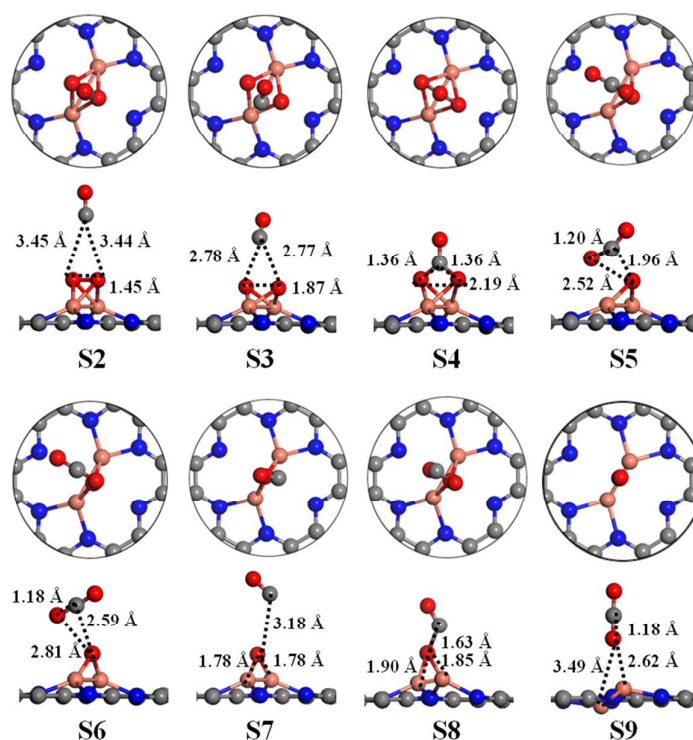


Figure 8. Atomic configurations of S2-S9 and the key structural parameters for CO oxidation via E-R mechanism on $\text{Cu}_2@C_2N$. The corresponding energy profiles were given in Figure 6 as marked in black. Color scheme: C, gray; N, blue; O, red; Cu, orange.

In the second E-R reaction route (E-R-2, the orange route in Figure 6 and atomic configurations in Figure 9), CO reacts with the activated O_2 (S2 in Figure 9, O–O bond distance 1.45 Å), one O of the adsorbed O_2 is lifted from Cu_2 by CO resulting in the O–O bond breakage and a newly formed C–O. Afterwards, the first CO_2 is directly produced rather than forming any intermediate (S4 in Figure 9). This process is exothermic (3.83 eV), and needs to pass an energy barrier of 0.52 eV (S3 in Figure 9), which is slightly lower compared to the first E-R route.

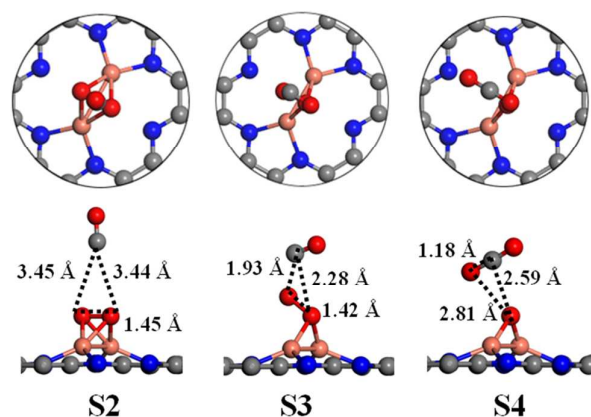


Figure 9. Atomic configurations of S2-S4 and the key structural parameters for CO oxidation via E-R-2 route on $\text{Cu}_2@\text{C}_2\text{N}$. The corresponding energy profiles were given in Figure 6 as marked in orange. Color scheme: C, gray; N, blue; O, red; Cu, orange.

The removal of the O^* by CO via E-R mechanism to form the second CO_2 ($\text{S7} \rightarrow \text{S8} \rightarrow \text{S9}$ in Figure 8) is more kinetically favorable, the barrier is 0.29 eV, very close to that of L-H mechanism (0.31 eV). The E-R reaction step is exothermic (1.28 eV).

Previous theoretical study showed that two CO molecules could assist O_2 scission and promote the CO oxidation.^{76,77} Furthermore, we considered a tri-molecular E-R (T-E-R) route (the blue route in Figure 6 and atomic configurations in Figure 10), in which two CO molecules approach the pre-adsorbed O_2 (side-on configuration) at the same time, and yield two CO_2 molecules simultaneously. The T-E-R pathway is kinetically more favorable compared to the above two E-R routes but less favorable than the L-H route, as indicated by the low barrier of 0.35 eV, and the exothermic reaction process (releasing 4.83 eV of heat). As a comparison, the O_2 dissociation on $\text{Cu}_2@\text{C}_2\text{N}$ is 0.56 eV and endothermic by 0.46 eV,⁵⁵ the two CO molecules' approaching assists the O–O bond breaking, and at the same time alternates the

scission reaction to a exothermic process.

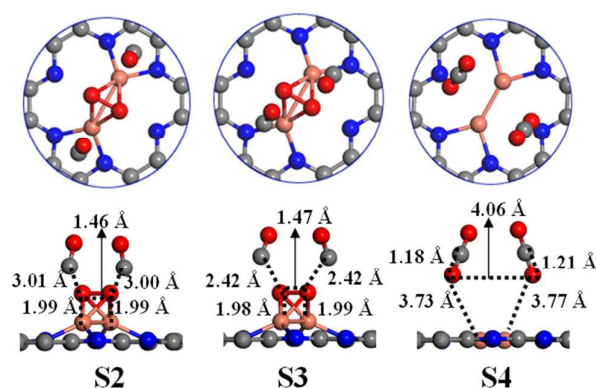


Figure 10. Atomic configurations of S2-S4 and the key structural parameters for CO oxidation via T-E-R mechanism on $\text{Cu}_2@\text{C}_2\text{N}$. The corresponding energy profiles were given in Figure 6 as marked in blue. Color scheme: C, gray; N, blue; O, red; Cu, orange.

In the proceeding sections, we systemically studied the mechanism of CO oxidation on $\text{Cu}_1@\text{C}_2\text{N}$ and $\text{Cu}_2@\text{C}_2\text{N}$. Clearly, the single-atom catalyst $\text{Cu}_1@\text{C}_2\text{N}$ already exhibits a high catalytic activity for CO oxidation, CO oxidation prefers the E-R mechanism, and the energy barriers for the first and second CO_2 formation are 0.53 and 0.21 eV, respectively. Remarkably, the bi-atom catalyst $\text{Cu}_2@\text{C}_2\text{N}$ displays even higher catalytic activity: for the first CO_2 formation, L-H mechanism is more kinetically preferred with a 0.17 eV activation barrier; while for the second CO_2 production, E-R mechanism is more favorable with a barrier of 0.29 eV.

3.4. Origin of the Superior Catalytic Performance of $\text{Cu}_2@\text{C}_2\text{N}$.

The superiority of the bi-atom catalyst $\text{Cu}_2@\text{C}_2\text{N}$ can be contributed to low barrier of the first CO_2 formation following the L-H mechanism, and such a favorable

reaction route can be further ascribed to the cooperation between the copper bi-atoms: On one hand, it provides “large” site for the coadsorption of CO and O₂, which is the prerequisite for the L-H mechanism; On the other hand, the copper dimer transfers more electrons to the adsorbate (0.34 and 0.90 e^- to CO and O₂, respectively, from Cu₂@C₂N, vs 0.13 and 0.38 e^- to CO and O₂ respectively from Cu₁@C₂N), and as a result, the adsorbed O₂ is highly activated as indicated by its elongated O–O bond length (1.45 Å on Cu₂@C₂N vs 1.28 Å on Cu₁@C₂N), which facilitates the formation of the intermediate OOCO*.

The second CO₂ formation on both Cu₁@C₂N and Cu₂@C₂N prefers the E-R mechanism, however, the reaction barrier on Cu₂@C₂N is slightly higher than that on Cu₁@C₂N (0.29 eV vs 0.21 eV). This mainly comes from the stronger adsorption strength of the O* with the Cu₂@C₂N. Whereas, the slightly higher barrier will not affect the overall performance of the Cu₂@C₂N over CO oxidation.

3.5. The Feasibility for Experimental Realization of Cu₁@C₂N and Cu₂@C₂N.

So far single metal atom on C₂N has not been synthesized yet, instead the Ru nanoparticles dispersed within the nitrogenated holes of C₂N⁷⁸ and Fe nanoparticles supported on C₂N⁷⁹ were obtained by Baek and co-workers. Considering the successful experimental synthesis of Ru and Fe nanoparticles supported by C₂N nanosheets and the recent achievements of single-atom catalysts, we believe that Cu can also be immobilized and uniformly embedded on the C₂N monolayer by immersing C₂N nanosheet in the dilute aqueous solution such as CuCl₂ with appropriate treatments.

Inspired by Ling *et al.*'s theoretical work,⁸⁰ using CuCl₂ as the metal precursor, we examined the feasibility for experimental realization of Cu₁@C₂N and Cu₂@C₂N

by computing the energy profile of the proposed synthetic route (Figures S6 and S7) and simulating the synthesis process by first principles molecular dynamics (FPMD) at 350 K in an NVT canonical ensemble (Figure S8). All the reaction steps can easily occur since they are either spontaneous (barrierless) or only slightly endothermic (Figure 7). In our FPMD simulations, the CuCl_2 in the solution is observed to adsorb on the C_2N , afterwards the Cl^- ions is desorbed. Within 0.3 ps, $\text{Cu}_1@C_2N$ is formed (Figure S8a,b), and the formation of $\text{Cu}_2@C_2N$ occurs at 0.5 ps of FPMD simulation (Figure S8c,d). Note that during the revision period of this work, Zhang *et al.*⁸¹ theoretically proposed that the transition metal anchored C_2N monolayer can be used as electrocatalysts for hydrogen and oxygen evolution reactions, and their FPMD simulations (10 ps at 800 K) revealed that both the $\text{Cu}_1@C_2N$ and $\text{Cu}_2@C_2N$ systems have very good thermal stabilities. Thus, we highly believe that the highly stable and efficient $\text{Cu}@C_2N$ catalysts could be synthesized by using CuCl_2 or other copper salts as a precursor.

4. Conclusions

In summary, by means of DFT computations, we explored the potential of using C_2N monolayer to anchor Cu_1 and Cu_2 as the bi-atom catalyst for CO oxidation. Both $\text{Cu}_1@C_2N$ and $\text{Cu}_2@C_2N$ exhibit thermodynamic good stabilities, and bi-atom catalyst (the Cu_2 dimer embedded in the porous C_2N monolayer) exhibits superior performance toward CO oxidation compared to single-atom catalyst $\text{Cu}_1@C_2N$: the O_2 molecule can be well activated on $\text{Cu}_2@C_2N$ as indicated by the stronger hybridization between the $3d$ states of Cu and the $2p$ states of adsorbed O_2 , which leads to the low barrier (0.17 eV) of the first CO_2 formation via L-H mechanism, in contrast, the barrier of producing the first CO_2 on $\text{Cu}_1@C_2N$ (0.53 eV) via E-R

mechanism is much higher; The removal of oxygen chemisorbed on $\text{Cu}_1@C_2N$ and $\text{Cu}_2@C_2N$ requires overcoming a barrier of 0.29 and 0.21 eV in term of E-R mechanism, respectively. Our comparative study suggests that the bi-atom catalyst, namely the copper dimer anchored on suitable substrate, is highly active for CO oxidation, which not only spans the single-atom catalysts, but also provides useful insights and guidelines to future theoretical and experimental investigations, and help promote the design and development of novel low-cost and efficient nanocatalysts.

Acknowledgement

This work was supported in China by the National Natural Science Foundation of China (No. 11704203) and the Startup Project of Inner Mongolia University in China, and in USA by NSF-CREST Center for Innovation, Research and Education in Environmental Nanotechnology (CIRE2N) (Grant Number HRD-1736093).

Electronic Supplementary Information

Top views of $\text{Cu}_2@C_2N$ structure transformation ($P1P1 \rightarrow P2P2$) after CO and O_2 adsorption; interaction between coadsorbed O_2 and CO with different configurations; PDOS of Cu-3d of $\text{Cu}_1@C_2N$ and $\text{Cu}_2@C_2N$; the details to examine the feasibility for experimental realization of $\text{Cu}_1@C_2N$ and $\text{Cu}_2@C_2N$. This material is available free of charge via the internet at <http://pubs.rsc.org>.

References:

-
- ¹ K. Liu, A. Wang, and T. Zhang, *ACS Catal.*, 2012, **2**, 1165.
 - ² M. Haruta, N. Yamada, T. Kobayashi and S. Iijima, *J. Catal.*, 1989, **115**, 301.
 - ³ K. Judai, S. Abbet, A. S. Wörz, U. Heiz and C. R. Henry, *J. Am. Chem. Soc.* **2004**,

126, 2732.

- ⁴ T. Schalow, B. Brandt, D. E. Starr, M. S. Laurin, K. Shaikhutdinov, Schauer mann, S.; J. Libuda and H.-J. Freund, *Angew. Chem. Int. Ed.*, 2006, **45**, 3693.
- ⁵ B. Qiao, A. Wang, X. Yang, L. F. Allard, Z. Jiang, Y. Cui, J. Liu, J. Li and T. Zhang, *Nature Chem.*, 2011, **3**, 634.
- ⁶ X. Yang, A. Wang, B. Qiao, J. Li, J. Liu and T. Zhang, *Acc. Chem. Res.*, 2013, **46**, 1740.
- ⁷ W. Zhang and W. Zheng, *Adv. Funct. Mater.*, 2016, **26**, 2988.
- ⁸ J. Liu, *ACS Catal.*, 2017, **7**, 34.
- ⁹ B. Bayatsarmadi, Y. Zheng, A. Vasileff and S.-Z. Qiao, *Small*, 2017, **13**, 1700191.
- ¹⁰ L. Wang, L. Huang, F. Liang, S. Liu, Y. Wang and H. Zhang, *Chin. J. Catal.*, 2017, **38**, 1528.
- ¹¹ F. Chen, X. Jiang, L. Zhang, R. Lang and B. Qiao, *Chin. J. Catal.*, 2018, **39**, 893.
- ¹² C. Zhu, S. Fu, Q. Shi, D. Du and Y. Lin, *Angew. Chem. Int. Ed.*, 2017, **56**, 13944.
- ¹³ Z. Li, D. Wang, Y. Wu and Y. Li, *Natl. Sci. Rev.*, 2018, nwy056.
- ¹⁴ J. Lin, A. Wang, B. Qiao, X. Liu, X. Yang, X. Wang, J. Liang, J. Li, J. Liu and T. Zhang, *J. Am. Chem. Soc.*, 2013, **135**, 15314.
- ¹⁵ J. Liang, J. Lin, X. Yang, A. Wang, B. Qiao, J. Liu, T. Zhang and J. Li, *J. Phys. Chem. C*, 2014, **118**, 21945.
- ¹⁶ H. Wei, X. Liu, A. Wang, L. Zhang, B. Qiao, X. Yang, Y. Huang, S. Miao, J. Liu and T. Zhang, *Nat. Comm.*, 2014, **5**, 5634.
- ¹⁷ B. Qiao, J. Liang, A. Wang, C. Xu, J. Li, T. Zhang and J. Liu, *Nano Research*, 2015, **8**, 2913.
- ¹⁸ J. Lin, B. Qiao, N. Li, L. Li, X. Sun, J. Liu, X. Wang, and T. Zhang, *Chem. Commun.*, 2015, **51**, 7911.
- ¹⁹ B. Qiao, J. X. Liang, A. Wang, J. Liu and T. Zhang, *Chin. J. Catal.*, 2016, **37**, 1580.
- ²⁰ J. Liang, X. Yang, A. Wang, T. Zhang and J. Li, *Catal. Sci. Technol.*, 2016, **6**, 6886.
- ²¹ B. Qiao, J. Lin, A. Wang, Y. Chen, T. Zhang and J. Liu, *Chin. J. Catal.*, 2015, **36**, 1505.
- ²² B. Qiao, J. Liu, Y. Wang, Q. Lin, X. Liu, A. Wang, J. Li, T. Zhang and J. Liu, *ACS Catal.*, 2015, **5**, 6249.
- ²³ M. Moses-DeBusk, M. Yoon, L. F. Allard, D. R. Mullins, Z. Wu, X. Yang, G. Veith, G. M. Stocks and C. K. Narula, *J. Am. Chem. Soc.*, 2013, **135**, 12634.

-
- ²⁴ D. Yang, S. Zhang, P. Xu, N. D. Browning, D. A. Dixon and B. C. Gates, *Chem. Eur. J.*, 2017, **23**, 2532.
- ²⁵ F. Li, Y. Li, X. C. Zeng and Z. Chen, *ACS Catal.*, 2015, **5**, 544.
- ²⁶ J. Liang, Q. Yu, X. Yang, T. Zhang, J. Li, *Nano Res.*, 2018, **11**, 1599.
- ²⁷ Q. Tang and Z. Zhou, *Prog. Mater. Sci.*, 2013, **58**, 1244.
- ²⁸ G. Zhu, Q. Sun, *Comp. Mater. Sci.*, 2016, **112**, 492.
- ²⁹ J. Shen, Y. Zhu, H. Jiang and C. Li, *Nano Today*, 2016, **11**, 483.
- ³⁰ W. Yang, X. Zhang and Y. Xie, *Nano Today*, 2016, **11**, 793.
- ³¹ C. Tan, X. Cao, X.-J. Wu, Q. He, J. Yang, X. Zhang, J. Chen, W. Zhao, S. Han, G.-H. Nam, M. Sindoro and H. Zhang, *Chem. Rev.*, 2017, **117**, 6225.
- ³² A. Bandyopadhyay, D. Ghosh and S. K. Pati, *J. Phys. Chem. Lett.*, 2018, **9**, 1605.
- ³³ S. Zhang, S. Guo, Z. Chen, Y. Wang, H. Gao, J. Gómez-Herrero, P. Ares, F. Zamora, Z. Zhu and H. Zeng, *Chem. Soc. Rev.*, 2018, **47**, 982.
- ³⁴ Z. Cai, B. Liu, X. Zou and H.-M. Cheng, *Chem. Rev.*, 2018, DOI: 10.1021/acs.chemrev.7b00536.
- ³⁵ M. Zeng, Y. Xiao, J. Liu, K. Yang and L. Fu, *Chem. Rev.*, 2018, DOI: 10.1021/acs.chemrev.7b00633.
- ³⁶ X. C. Wang, K. Maeda, A. Thomas, K. Takanabe, G. Xin, J. M. Carlsson, K. Domen and M. Antonietti, *Nat. Mater.*, 2009, **8**, 76.
- ³⁷ K. Tahara, Y. Yamamoto, D. E. Gross, H. Kozuma, Y. Arikuma, K. Ohta, Y. Hoizumi, Y. Gao, Y. Shimizu, S. Seki, K. Kamada, J. S. Moore and Y. Tobe, *Chem. A Eur. J.*, 2013, **19**, 11251.
- ³⁸ G. Li, Y. Li, H. Liu, Y. Guo, Y. Li and D. Zhu, *Chem. Commun.*, 2010, **46**, 3256.
- ³⁹ J. Mahmood, E. K. Lee, M. Jung, D. Shin, I.-Y. Jeon, S.-M. Jung, H.-J. Choi, J.-M. Seo, S.-Y. Bae, S. D. Sohn, N. Park, J. H. Oh, H.-J. Shin and J.-B. Baek, *Nat. Commun.*, 2015, **6**, 6486.
- ⁴⁰ M. Abel, S. Clair, O. Ourdjini, M. Mossoyan and L. Porte, *J. Am. Chem. Soc.*, 2011, **133**, 1203.
- ⁴¹ Z. Shi, J. Liu, T. Lin, F. Xia, P. L. Liu and N. Lin, *J. Am. Chem. Soc.*, 2011, **133**, 6150.
- ⁴² T. Kambe, R. Sakamoto, K. Hoshiko, K. Takada, M. Miyachi, J. H. Ryu, S. Sasaki, J. Kim, K. Nakazato and T. Takata, *J. Am. Chem. Soc.*, 2013, **135**, 2462.
- ⁴³ (a) G. Vilé, D. Albani, M. Nachtegaal, Z. Chen, D. Dontsova, M. Antonietti, N.

- López and J. Pérez-Ramírez, *Angew. Chem. Int. Ed.*, 2015, **54**, 11265. (b) Z. Chen, S. Mitchell, E. Vorobyeva, R. K. Leary, R. Hauert, T. Furnival, Q. M. Ramasse, J. M. Thomas, P. A. Midgley, D. Dontsova, M. Antonietti, S. Pogodin, N. López and J. Pérez-Ramírez, *Adv. Funct. Mater.*, 2017, **27**, 1605785.
- ⁴⁴ X. Li, P. Cui, W. Zhong, J. Li, X. Wang, Z. Wang and J. Jiang, *Chem. Commun.*, 2016, **52**, 13233.
- ⁴⁵ D. Ma, T. Li, Q. Wang, G. Yang, C. He, B. Ma and Z. Lu, *Carbon*, 2015, **95**, 756.
- ⁴⁶ D. Ma, Q. Wang, X. Yan, X. Zhang, C. He, D. Zhou, Y. Tang, Z. Lu and Z. Yang, *Carbon*, 2016, **105**, 463.
- ⁴⁷ Z. Wang, Z. Yu and J. Zhao, *Phys. Chem. Chem. Phys.*, 2018, DOI: 10.1039/C8CP01215F.
- ⁴⁸ Y. Wang, Y. Li and Z. Chen, *Nanoscale*, 2015, **7**, 11633.
- ⁴⁹ X. Wang, B. Wang, J. Zhong, F. Zhao, N. Han, W. Huang, M. Zeng, J. Fan and Y. Li, *Nano Res.*, 2016, **9**, 1497.
- ⁵⁰ I. G. Powers and C. Uyeda, *ACS Catal.*, 2017, **7**, 936.
- ⁵¹ O. Matsushita, V. M. Derkacheva, A. Muranaka, S. Shimizu, M. Uchiyama, E. A. Luk'yanets and N. Kobayashi, *J. Am. Chem. Soc.*, 2012, **134**, 3411.
- ⁵² H. Shen, Y. Li and Q. Sun, *J. Phys. Chem. C*, 2017, **121**, 3963.
- ⁵³ Z. He, K. He, A. W. Robertson, A. I. Kirkland, D. Kim, J. Ihm, E. Yoon, G.-D. Lee and J. H. Warner, *Nano Lett.*, 2014, **14**, 3766.
- ⁵⁴ H. Yan, Y. Lin, H. Wu, W. Zhang, Z. Sun, H. Cheng, W. Liu, C. Wang, J. Li, X. Huang, T. Yao, J. Yang, S. Wei, and J. Lu, *Nat. Comm.*, 2017, **8**, 1070.
- ⁵⁵ X. Li, W. Zhong, P. Cui, J. Li and J. Jiang, *J. Phys. Chem. Lett.*, 2016, **7**, 1750.
- ⁵⁶ J. P. Perdew, K. Burke and M. Ernzerhof, *Phys. Rev. Lett.*, 1996, **77**, 3865.
- ⁵⁷ P. E. Blöchl, *Phys. Rev. B*, 1994, **50**, 17953.
- ⁵⁸ G. Kresse and J. Furthmüller, *Phys. Rev. B*, 1996, **54**, 11169.
- ⁵⁹ H. J. Monkhorst and J. D. Pack, *Phys. Rev. B*, 1976, **13**, 5188.
- ⁶⁰ G. Henkelman, B. P. Uberuaga and H. Jónsson, *J. Chem. Phys.*, 2000, **113**, 9901.
- ⁶¹ G. Henkelman, A. Arnaldsson and H. Jónsson, *Comput. Mater Sci.*, 2006, **36**, 354.
- ⁶² (a) L. Giordano, C. D. Valentin, J. Goniakowski and G. Pacchioni, *Phys. Rev. Lett.*, 2004, **92**, 096105; (b) A. D. Vitto and G. Pacchioni, *J. Phys. Chem. B*, 2005, **109**, 8040.
- ⁶³ J. Wellendorff, K. T. Lundgaard, A. Møgelhøj, V. Petzold, D. D. Landis, J. K.

-
- Nørskov, T. Bligaard and K. W. Jacobsen, *Phys. Rev. B*, 2012, **85**, 235149.
- ⁶⁴ S. Grimme, *J. Comput. Chem.*, 2006, **27**, 1787.
- ⁶⁵ B. Hammer and J. K. Nørskov, *Nature*, 1995, **376**, 238.
- ⁶⁶ B. Hammer and J. K. Nørskov, *Surf. Sci.*, 1995, **343**, 211.
- ⁶⁷ B. Hammer, Y. Morikawa and J. K. Nørskov, *Phys. Rev. Lett.*, 1996, **76**, 2141.
- ⁶⁸ B. Hammer and J. K. Nørskov, *Adv. Catal.*, 2000, **45**, 71.
- ⁶⁹ H. Xin and S. Linic, *J. Chem. Phys.*, 2010, **132**, 221101.
- ⁷⁰ M. T. Gorzkowski and A. Lewera, *J. Phys. Chem. C*, 2015, **119**, 18389.
- ⁷¹ H. Xu, D. Cheng, D. Cao and X. C. Zeng, *Nat. Catal.*, 2018, **1**, 339.
- ⁷² Y. H. Lu, M. Zhou, C. Zhang and Y. P. Feng, *J. Phys. Chem. C*, 2009, **113**, 20156.
- ⁷³ E. H. Song, Z. Wen and Q. Jiang, *J. Phys. Chem. C*, 2011, **115**, 3678.
- ⁷⁴ Y. Li, Z. Zhou, G. Yu, W. Chen and Z. Chen, *J. Phys. Chem. C*, 2010, **114**, 6250.
- ⁷⁵ F. Li, J. Zhao and Z. Chen, *J. Phys. Chem. C*, 2012, **116**, 2507.
- ⁷⁶ C. Liu, Y. Tan, S. Lin, H. Li, X. Wu, L. Li, Y. Pei and X. C. Zeng, *J. Am. Chem. Soc.*, 2013, **135**, 2583.
- ⁷⁷ K. Mao, L. Li, W. Zhang, Y. Pei, X. C. Zeng, X. Wu and J. Yang, *Sci Rep.*, 2014, **4**, 5441.
- ⁷⁸ J. Mahmood, F. Li, C. Kim, H.-J. Choi, O. Gwon, S.-M. Jung, Jeong-MinSeo, S.-J. Cho, Y.-W. Ju, H. Y. Jeong, G. Kim and J.-B. Baek, *Nat. Nanotechnol.*, 2017, **12**, 441.
- ⁷⁹ J. Mahmood, F. Li, S.-M. Jung, M. S. Okyay, I. Ahmad, S.-J. Kim, N. Park, H. Y. Jeong and J.-B. Baek, *Nano Energy*, 2018, **44**, 304.
- ⁸⁰ C. Ling, L. Shi, Y. Ouyang, X. C. Zeng and J. Wang, *Nano Lett.*, 2017, **17**, 5133.
- ⁸¹ X. Zhang, A. Chen, Z. Zhang, M. Jiao and Z. Zhou, *J. Mater. Chem. A*, 2018, **6**, 11446.

TOC

